SURFACE AND INTERFACE ANALYSIS
Surf. Interface Anal. **27**, 361–367 (1999)

Measuring and Modifying the Electric Surface Potential Distribution on a Nanometre Scale: a Powerful Tool in Science and Technology

H. O. Jacobs and A. Stemmer*
Nanotechnology Group, Institute of Robotics, Swiss Federal Institute of Technology, CH-8092 Zurich, Switzerland

The combination of atomic force microscopy (AFM) and Kelvin probe technology is a powerful tool to obtain high-resolution maps of the electric surface potential distribution on conducting and non-conducting samples. We show that potential maps of composite metal films and semiconductors show a clear chemical contrast and can be used to differentiate between different materials with a lateral resolution of a few 10 nm. Because AFM tips are not point-like structures, we establish a simple model to correlate the measured quantities with the true surface potential distribution, and compare numerical simulations of the three-dimensional tip–specimen model with experimental data from test structures. For the first time, we combine the electrostatic surface potential and the topography data to derive the local electrostatic field strength on active transistors. Using suitable substrates, trapped surface charges can be generated by applying short voltage pulses between the tip and the sample surface. These surface charges can be detected in the electric surface potential image and might be used as bits in new data storage systems or as target sites in self-assembly processes.

KEYWORDS: surface potential; contact potential; Kelvin probe; SPM; AFM; photo-voltage; trapped surface charges; chemical contrast; data storage; electric field strength; HEMT; heterostructures

INTRODUCTION

The ability to image directly the electric surface potential distribution on a nanometre scale leads to a powerful new analytical tool to characterize conducting and non-conducting surfaces by their electrical properties. For instance, junctions between different materials, locations of electric short cuts and the distribution of the electric field intensity are all of major interest in semiconductor device design, as well as failure analysis.

High-resolution mapping of local electric potential distributions on a nanometre scale became feasible with the introduction of scanning tunneling microscopy.[1,2] Adaptation of atomic force microscopy (AFM) to electric potential measurements[3,4] immediately broadened the application range to non-conducting samples, because now the tip could be kept close to the surface without the necessity of a tunneling current. In particular, variations of Kelvin probe force microscopy[5–7] (KFM) have evolved into reliable tools to characterize specimens ranging from semiconductor devices[8,9] to biological samples.[10,11]

We present an overview of the main aspects involved in measuring and modifying electric surface potentials using KFM. First, we show that KFM provides a clear material contrast on composite structures where electron diffusion between different materials creates associated surface potentials. Because the magnitude of the detected electric potential critically depends on the size of the material patches, their surroundings and the probe geometry, a clear understanding of the contrast transfer mechanism in KFM is required to enable a quantitative analysis and interpretation of potential images. A simple model that takes into account the various contributions to the capacitance between tip and sample allows us to correlate the measured quantities with the true surface potential distribution. We compare numerical simulations of the KFM contrast transfer characteristics for steps in the electric surface potential with measured data. The knowledge of this contrast transfer mechanism will permit a combination of high-resolution surface topography and electric potential data that is likely to facilitate significantly the development of new and improved semiconductor devices. As an example in this direction, we derive the electrostatic field strength from the topography and the electrostatic surface potential to find, on active high-electron-mobility transistors, locations of maximum field intensity. Finally, KFM can also be used to generate and detect trapped surface charges. These localized charges are generated by applying short voltage pulses between the tip and suitable substrates[12] and have been suggested to serve as bits in new data storage systems[13–16] or as target sites in self-assembly processes.[12]

INSTRUMENT SET-UP

Our KFM miroscope[17] is based on a modified commercial atomic force microscope (NanoScope® IIIa MultiMode™ with Extender™ Electronics Module, Digital Instruments, USA) where topography and electric surface potential are measured sequentially using the lift-mode technique to minimize cross-talk.[17] To this

* Correspondence to: A. Stemmer, Nanotechnology Group, Institute of Robotics, Swiss Federal Institute of Technology, CH-8092 Zurich, Switzerland. E-mail: stemmer@ifr.mart.ethz.ch

CCC 0142–2421/99/050361–07 $17.50

Received 15 September 1998
Accepted 12 November 1998

end, we first acquire the surface topography of a single line in TappingMode™ and then immediately retrace this topography over the same line at a set lift-height (typically 15 nm) from the sample surface to measure the surface potential distribution. Images are obtained by repeating this procedure for each line along the slow-scan axis. The electric surface potential is acquired using the standard KFM feedback loop, which was slightly modified to increase the sensitivity and stability of the feedback.[18]

All measurements are taken in air at ambient pressure and humidity. Under these conditions the local surface potential is affected by contamination, oxide layers or trapped surface charges.[5] For our experiments we used commercially available n-doped silicon tapping-mode tips from a single wafer (Nanoprobes, Digital Instruments, USA). These semiconducting tips must be connected electrically via metal contact pads. We used InGa and colloidal silver pads, which are easily applied to the substrate supporting the cantilever and have a low enough differential contact resistance [$(dI/dU)|_{U=0\,V} = 350\ \Omega$ and 2.2 kΩ, respectively].[18]

Because the tip geometry defines the resolution in KFM,[19] we determined the relevant parameters using a calibrated scanning electron microscope. All investigated tips had the same opening angle $\alpha = 34°$ and tip length $l = 21\ \mu m$. At the base of the tip the cantilever measured 18 μm in width. The apex radius r_a of the tips varied between 10 and 200 nm.

MATERIAL CONTRAST IN KFM

Electrons in a material have a specific chemical binding energy. When two different materials are connected electrically, electrons flow from the material with the smaller work function (weak binding) to the material with the higher work function [strong binding; Fig. 1(a)]. This diffusion current builds up an electric double layer at the interface, resulting in an electrostatic potential difference U_c (contact potential, CP) between the two materials. At equilibrium, the electrostatic force cancels the diffusion force in the interface and the contact potential equals the difference of the two work functions Φ_{m1} and Φ_{m2} [Fig. 1(b)].

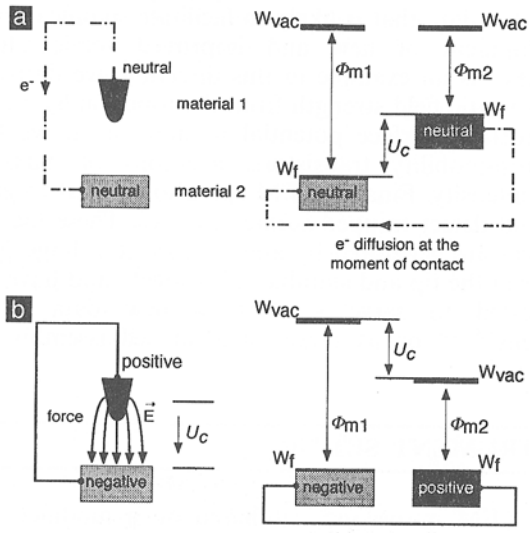

Figure 1. Energy diagrams of sample and conducting tip explaining the material contrast in KFM. (a) Neutral tip and sample before being electrically connected. (b) Interaction force and electrostatic potential difference after contact and electron diffusion (W_{vac}, vacuum energy level; W_f, fermi energy; ϕ_{mi}, work function of material i; U_c, contact potential between material 1 and 2).

Outside of the bulk materials, the different surface potentials cause electrostatic forces between the surfaces, i.e. tip and sample [Fig. 1(b)]. On specimens consisting of different materials, the attractive electrostatic tip-force varies locally and becomes

$$F_z = \frac{1}{2} \cdot \frac{dC}{dz} \cdot U_c^2(x), \tag{1}$$

where C is the tip–sample compacitance and U_c is the CP at the actual tip location.

In KFM, an a.c. voltage $U_{ac}\cos(\omega t)$, typically 10 Vpp, tuned to the first resonance of the cantilever and the adjustable dc offset Φ_{dc}, is applied between the conducting AFM tip and the sample electrode (Fig. 2). The electrostatic force interaction between the two electrodes [Eqn (1)] then becomes

$$F_z = \frac{1}{2} \cdot \frac{dC}{dz} [U_c(x) - \Phi_{dc} - U_{ac}\cos(\omega t)]^2 \tag{2}$$

with spectral components at the d.c., ω and 2ω.

The ω component

$$F_\omega = -\frac{dC}{dz} [(U_c(x) - \Phi_{dc})U_{ac}] \tag{3}$$

of the resulting electrostatic force is detected by a lock-in amplifier, and a feedback circuit controls the d.c. tip potential until the ω component of the electrostatic force is compensated. When the ω component of the electrostatic force vanishes ($F_\omega = 0$), the d.c. tip potential Φ_{dc} compensates the local contact potential U_c ($\Phi_{dc} = U_c$). Thus, the contact potential distribution (CPD) is obtained by mapping the controlled d.c. tip potential while the tip is scanned at a certain lift-height (we typically use 15 nm) above the surface.

In the following we demonstrate the potential of KFM on perforated metal films[17,19] and several types of heterostructures, such as vertical cavity lasers,[17] pin-junctions and GaAs/GaInP-junctions. Figure 3 displays the topography and KFM potential of a perforated Pt–C film on top of a Ta–W film, and vice versa. The

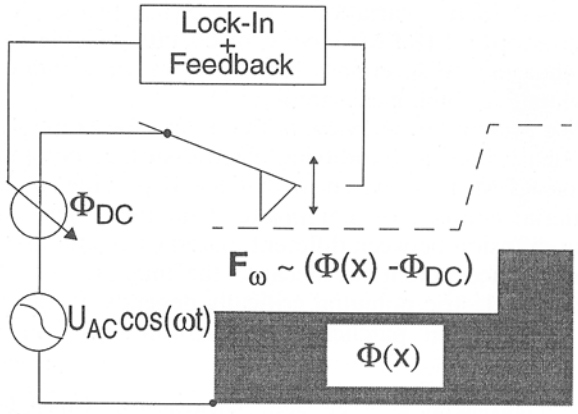

Figure 2. KFM principle to measure the surface potential distribution $\phi(x)$ (see text for details).

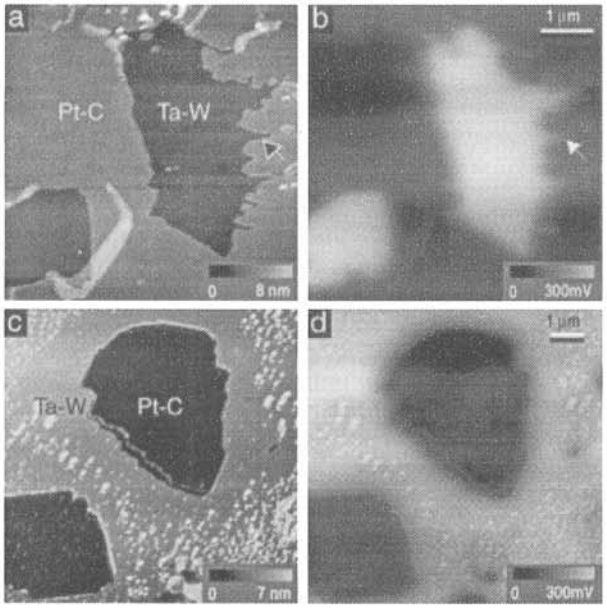

Figure 3. Topography and surface potential between different metal films. The top row shows topography (a) and surface potential (b) for the perforated Pt–C film on top of Ta–W. Features down to ~80 nm can be seen in the potential image (white arrow). The bottom row shows topography (c) and surface potential (d) for the perforated Ta–W film on top of Pt–C. All potential images were taken at 15 nm lift-height.

films are 5 nm thick and were evaporated on glass substrates. The Ta–W always appears positive by ~300 mV with respect to Pt–C in the potential images, independent of its location, i.e. top or bottom layer.

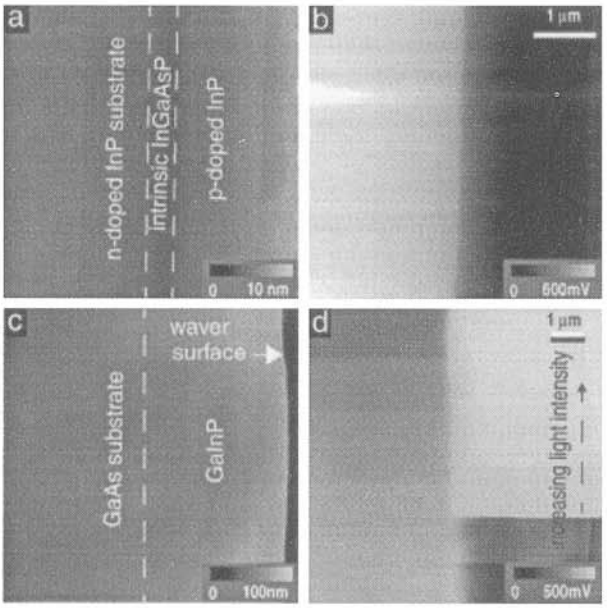

Figure 4. Topography and surface potential of the cleaved surface of epitaxially grown heterostructures. Topography (a) and surface potential (b) of a pin-junction. The pin-junction is only visible in the potential image. Topography (c) and surface potential (d) of a GaAs/GaInP junction when the waver surface is illuminated with step-wise increasing (bottom to top) light intensities. Under illumination, light-induced charge carriers diffuse through the junction and, therefore, change the actual surface potential distribution. This effect is only visible in the KFM potential image (d). All potential images were taken at 15 nm lift-height.

Thus, with this material contrast we can clearly distinguish between areas of different chemical composition. Furthermore, surface features down to several tens of nanometres in size can be detected in the potential image [arrows in Figs 3(a) and 3(b)].

The topography and KFM potential of cleaved surfaces of different heterostructures are shown in Fig. 4. Figure 4(a) shows the cross-section through a pin-junction (n-doped InP substrate with 0.3 µm epitaxially grown intrinsic InGaAsP and 1.78 µm p-doped InP on top). The potential image [Fig. 4(b)] reveals a clear step of ~400 mV between the n-doped and p-doped region, which cannot be seen in the topography image. Figure 4(c) shows the cross-section through GaAs substrate with a 4.8 µm thick epitaxially grown GaInP on top. While scanning the cleaved side, the waver surface was illuminated with a cold light source (KL 1500, halogen tungsten lamp, Schott GmbH) and the intensity was varied stepwise. Under illumination, light-induced charge carriers diffuse through the interface and thereby change the potential difference between both materials. Without illumination, GaInP appears negative by 150 mV with respect to GaAs, whereas at high illumination intensities the GaInP surface layer becomes positive by 220 mV with respect to GaAs.

RESOLUTION AND CONTRAST TRANSFER IN KFM

Theory

To correlate the actual surface potential distribution with the measured quantities, we model our KFM set-up as a sample surface consisting of n electrodes of constant potential $\Phi_i = U_{b,i} + U_{c,i}$, where $U_{b,i}$ represents an external bias voltage to the ith electrode and $U_{c,i}$ represents the contact potential between the tip an the ith electrode (Fig. 5). Under these conditions, the electrostatic interactions between the tip and each individual electrode can be represented by the mutual

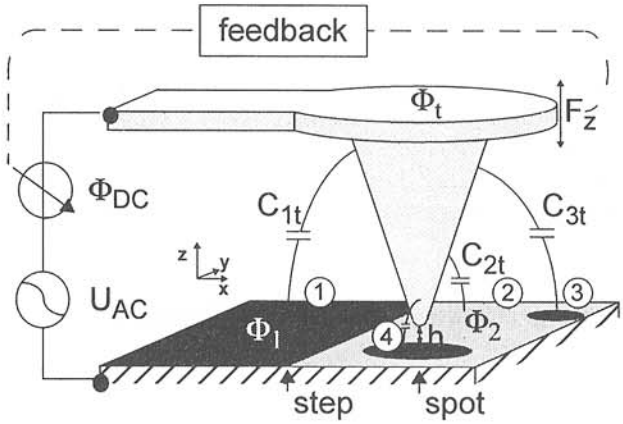

Figure 5. Model of the KFM set-up: system of ideal conductors with electrostatic interactions represented by mutual capacitances C_{ij}.

capacitances C_{ij}. Applying the external a.c. voltage with adjustable d.c. offset to the conducting tip $[\Phi_t = \Phi_{dc} + U_{ac}\cos(\omega t)]$, the ω component of the electrostatic force becomes

$$F_\omega = -\sum_{i=1}^{n} C'_{it}(x)(\Phi_i - \Phi_{dc})U_{ac} \quad (4)$$

where $C'_{it} = \partial C_{it}/\partial z$ is the derivative of the mutual capacitance between the tip and the ith electrode at the actual tip location.[19]

Kelvin probe force microscopy detects F_ω, and a feedback adjusts the d.c. potential offset, Φ_{dc} potential offset, Φ_{dc}, until F_ω vanishes. Setting $F_\omega = 0$, we obtain

$$\Phi_{dc} = \frac{\sum_{i=1}^{n}(C'_{it}\Phi_i)}{\sum_{i=1}^{n} C'_{it}} \quad (5)$$

for the measured KFM potential. Equation (5) demonstrates that resolution and accuracy in KFM are defined by the electrostatic coupling between the tip and the different surface regions. Therefore, the measured KFM potential Φ_{dc} does not exactly match the surface potential below the tip, rather it is a weighted average over all potentials Φ_i on the surface, the derivatives of the capacitances, C'_{it}, being the weighting factors.[17]

Subdividing an infinitely large and perfectly flat surface with the potential distribution $\Phi(x, y)$ into equally sized elements of area $\Delta x \Delta y$ at locations $\{x_i, y_i\}$, the KFM potential [Eqn (5)] as a function of the tip location (x_t, y_t) can be expressed as

$$\Phi_{dc}(x_t, y_t) = \sum_{j=-\infty}^{\infty}\sum_{i=-\infty}^{\infty}\left[\frac{C'(x_i - x_t, y_j - y_t)}{C'_{tot}} \cdot \Phi(x_i, y_j)\right] \quad (6)$$

and because the denominator of Eqn (6) is independent of the lateral tip location for an infinitely large surface, we obtain

$$\Phi_{dc}(x_t, y_t) = \int_{-\infty}^{\infty}\int_{-\infty}^{\infty} h(x - x_t, y - y_t)\Phi(x, y)\,dx\,dy$$

$$h(x - x_t, y - y_t) = \lim_{\Delta x, \Delta y \to 0}\left[\frac{C'(x_i - x_t, y_i - y_t)}{C'_{tot}\,\Delta x \Delta y}\right] \quad (7)$$

for infinitely small surface elements Δx and Δy.

Equation (7) shows that detected KFM-potential maps $\Phi_{dc}(x, y)$ of flat, infinitely large surfaces are two-dimensional convolutions of the actual surface potential distribution $\Phi(x, y)$ with the corresponding transfer function $h(x, y)$, which is defined by the tip geometry.

Computer simulations and measured response for a potential step

To compare our model, which correlates the measured KFM potential with the true surface potential distribution [Eqn (5)], with experimental data we first calculated the expected response when the tip is scanned across an ideal potential step. The step potential was modelled as half-plane $x < 0$ with potential Φ_1 and half-plane $x > 0$ with potential Φ_2. In this case, Eqn (5) translates into

$$\Phi_{dc} = \frac{C'_{1t}\Phi_1 + C'_{2t}\Phi_2}{C'_{1t} + C'_{2t}}, \quad (8)$$

where the values C'_{1t} and C'_{2t} depend on geometry parameters, i.e. the location and geometry of the tip. The mutual capacitances C_{1t} and C_{2t} are defined by the actual tip charge Q_t. For the boundary condition $\{\Phi_t = \Phi_2 = 0,\ \Phi_1 \neq 0\}$, $C_{1t} = -Q_t(z)/\Phi_1$; similarly, $C_{2t} = -Q_t(z)/\Phi_2$ for $\{\Phi_t = \Phi_1 = 0, \Phi_2 \neq 0\}$.

The derivatives of the capacitances $\{C'_{1t},\ C'_{2t}\}$ required to predict the potential Φ_{dc} [Eqn (8)] were obtained numerically via the difference in capacitance due to a small height change Δz of the tip

$$C'_{1t} = \frac{C_{1t}(z + \Delta z) - C_{1t}(z)}{\Delta z},$$

$$C'_{2t} = \frac{C_{2t}(z + \Delta z) - C_{2t}(z)}{\Delta z}. \quad (9)$$

Thus, the task of determining the derivatives of the mutual capacitances, $C'_{it}(z)$, was reduced to the problem of calculating the tip charge Q_t for each electrode configuration and each boundary condition.[19] This required a highly accurate knowledge of the three-dimensional electrostatic field distribution, which was calculated via a multiple multipole program MMP.[20–22]

Figure 6 displays a particular tip–sample geometry and the associated electrostatic field distributions (plane $y = 0$) obtained by MMP for the step-potential. The field vectors and the contours of constant potential clearly demonstrate that the boundary conditions are met for the entire electrode configuration. We approximated the actual tip geometry by a conical tip with apex radius, opening angle and tip length matching the measured parameters of the tips used (see above). The cantilever was modelled as a disc of diameter $d_{top} = 18$ μm and all parts were considered to have zero resis-

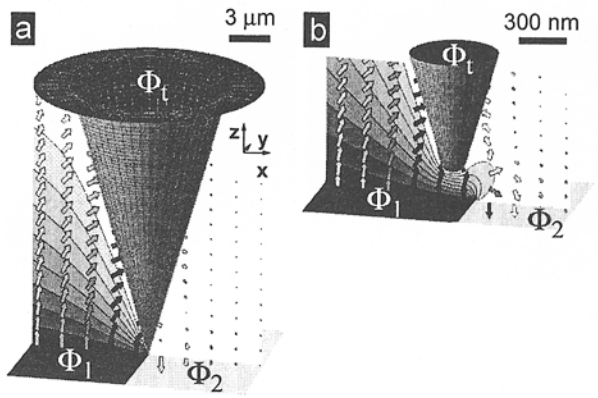

Figure 6. Modelled tip and electrostatic field distribution for a step potential located below the tip. Tip length $l = 21$ μm, opening angle $\alpha = 34°$, apex radius $r_a = 100$ nm and cantilever width $d_{top} = 18$ μm match the dimensions of the tip used in our experiments (Fig. 7). The tip is positioned 150 nm beside and 150 nm above the potential step (b). Boundary condition: $\{\Phi_t = \Phi_2 = 0, \Phi_1 \neq 0\}$.

tivity. The field distribution shown in Fig. 6 represents only one point of the response characteristics. For the total system response shown in Fig. 7(c), a series of simulations was run with different tip locations.

To validate the modelled step response, we determined experimentally the CPD of a perforated Pt–C film on a GaAs substrate.[19] Figure 7 displays the topography and KFM potential of the structure. The measured potential difference between the 8 nm thick Pt–C film and the GaAs substrate is 540 mV. We measured the KFM potential along the three lines indicated in (b), normalized the data using the 540 mV potential difference between Pt–C and GaAs and calculated the mean response curves. Figure 7(c) compares these mean responses (solid lines) with the modelled step responses (discrete points) for different tip–sample separations h. Evidently, we obtain good agreement between the predicted step response and the measured data. Near the transition ($|s| < 500$ nm) the predicted response is slightly steeper than the experimentally observed response. This is not surprising, because our simulations are based on an ideal step potential. In an actual potential distribution the transition is defined by the length of the space charge region, which always has a finite length.

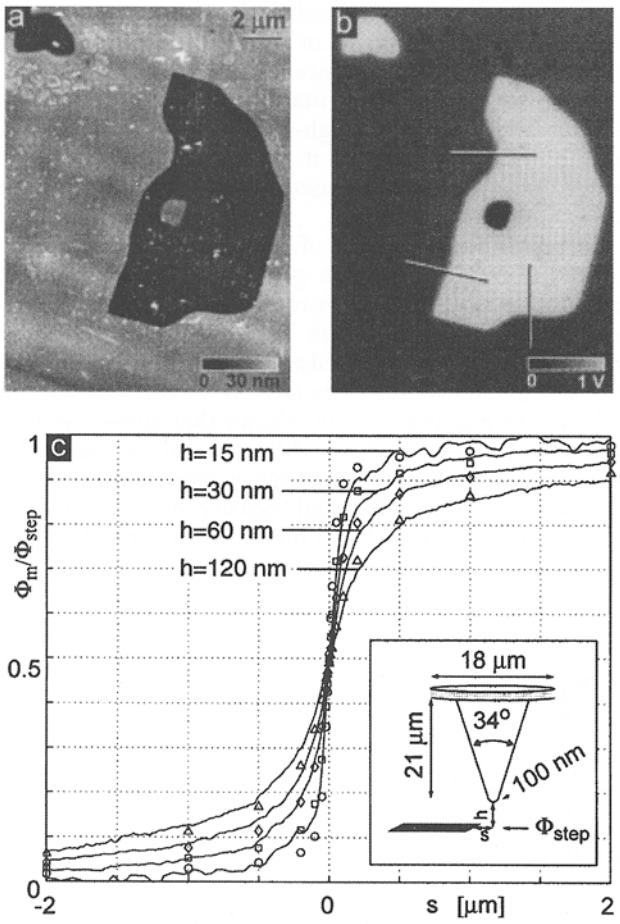

Figure 7. Measured and modelled step response. Topography (a) and KFM potential (b) for the 8 nm thick perforated Pt–C film on top of GaAs. (c) Step response (solid line) averaged from measurements along the three lines indicated in (b) and normalized to the maximum potential difference between the Pt–C film and the GaAs substrate. Open symbols mark the modelled step response calculated with a tip (inset) matching the characteristics of the actual tip used in the experiment. [Reprinted with permission from H. O. Jacobs, P. Leuchtmann, O. J. Homan and A. Stemmer, *J. Appl. Phys.* **84**, 1168 (1998). Copyright 1998 American Institute of Physics.]

Studies of the effect of the tip geometry on resolution and contrast transfer showed that slightly blunt tips (apex radius of typically 100 nm) produce a steeper response than tips with a 10 nm apex radius. Additionally, we found that high-resolution KFM images are only obtained with long and slender tips, provided that the tip apex is not too small.[19]

THE ELECTROSTATIC FIELD STRENGTH ON A HIGH-ELECTRON-MOBILITY TRANSISTOR

Both externally applied voltages and internal voltages due to the contact potential between different materials cause electric fields. The tangential component $\boldsymbol{E}_t$ along the sample surface can be calculated from the surface potential distribution Φ and the topography $Z(x, y)$ of the structure. Considering two points on the sample surface with potentials Φ at location $[x, y, Z(x, y)]$ and potential $\Phi + d\Phi$ at location $[x + dx, y + dy, Z(x + dx, y + dy)]$, the electrostatic potential difference $d\Phi$ between both points is given by

$$d\Phi = \boldsymbol{E}\, d\boldsymbol{s}, \tag{10}$$

where $\boldsymbol{E}\, d\boldsymbol{s}$ is the scalar product between the electrostatic field vector $\boldsymbol{E}$ and the incremental distance vector $d\boldsymbol{s}$ between both points.

If we choose $d\boldsymbol{s}_x = [dx, 0, Z(x + dx, y) - Z(x, y)]$ and $d\boldsymbol{s}_y = [(0, dy, Z(x, y + dy) - Z(x, y)]$, we find

$$\boldsymbol{E}_t = \frac{\Phi[x + dx, y, Z(x + dx, y)] - \Phi[x, y, Z(x, y)]}{\sqrt{dx^2 + [Z(x + dx, y) - Z(x, y)]^2}} \frac{d\boldsymbol{s}_x}{|d\boldsymbol{s}_x|} + \frac{\Phi[x, y + dy, Z(x, y + dy)] - \Phi[x, y, Z(x, y)]}{\sqrt{dy^2 + [Z(x, y + dy) - Z(x, y)]^2}} \frac{d\boldsymbol{s}_y}{|d\boldsymbol{s}_y|} \tag{11}$$

for the tangential component of the electrostatic field $\boldsymbol{E}_t$. Generally, $\boldsymbol{E}_t$ has three components, in the x, y and z directions

$$E_{tx} = \frac{\Phi[x + dx, y, Z(x + dx, y)] - \Phi[x, y, Z(x, y)]}{dx^2 + [Z(x + dx, y) - Z(x, y)]^2} dx$$

$$E_{ty} = \frac{\Phi[x, y + dy, Z(x, y + dy)] - \Phi[x, y, Z(x, y)]}{dy^2 + [Z(x, y + dy) - Z(x, y)]^2} dy$$

$$E_{tz} = \frac{\Phi[x + dx, y, Z(x + dx, y)] - \Phi[x, y, Z(x, y)]}{dx^2 + [Z(x + dx, y) - Z(x, y)]^2} \times [Z(x + dx, y) - Z(x, y)] + \frac{\Phi[x, y + dy, Z(x, y + dy)] - \Phi[x, y, Z(x, y)]}{dy^2 + [Z(x, y + dy) - Z(x, y)]^2} \times [Z(x, y + dy) - Z(x, y)], \tag{12}$$

Figure 8 displays the topography, surface potential and field intensity distribution $|\boldsymbol{E}_t| = \sqrt{E_{tx}^2 + E_{ty}^2 + E_{tz}^2}$

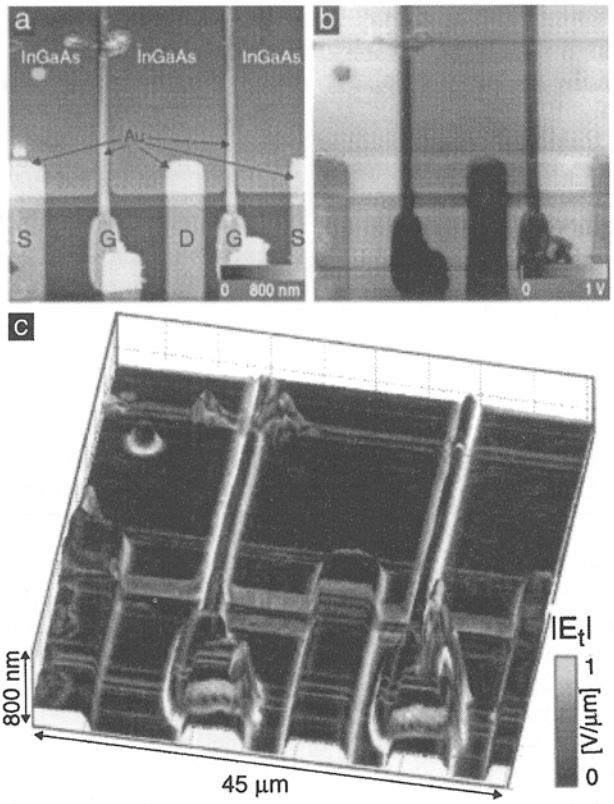

Figure 8. Topography (a), surface potential (b) and tangential electric field intensity (c) for two externally biased high-electron-mobility transistors. The external bias $U_{ds} = U_{gs} = -0.7$ V was applied by Au contact metallizations visible at the bottom of the device. Highest field intensities occur on both sides of the 1.2 µm wide Au-gate fingers. These fields originate from the internal contact potential difference of approx. −300 mV between the Au gate and the surrounding InGaAs cap layers, and the external bias potential. A defect can be seen in the upper left part of the device. The potential data were acquired at 20 nm lift-height. Letters S, G and D denote source, gate and drain, respectively.

on two externally biased high-electron-mobility transistors. For the device shown, the gate-source and drain-source voltage was −0.7 V. It can be seen that the highest intensity values appear between gate and source. Typically, the gate region is also the location where electric breakdown occurs.

TRAPPED SURFACE CHARGES

Influence on the surface potential

In many practical experiments, particularly at ambient pressure, surfaces are not perfectly clean. Surface contamination, oxides and isolated charges change the local surface potential distribution and hence become visible in the KFM potential image. To investigate the impact of an isolated surface charge on the local surface potential distribution, we consider the following situation: the isolated charge Q is located at a distance D below the sample surface ($z = 0$). The sample fills up the half-space $z < 0$ and has a dielectric constant $\varepsilon_m \varepsilon_0$. Then the field distribution can be calculated analytically by using an image charge $Q_{im} = (\varepsilon_m - 1)/(\varepsilon_m + 1)Q$, which is located at a distance D above the sample surface.[23] We obtain

$$\Phi(\rho) = \frac{Q}{2\pi\varepsilon_0(\varepsilon_m + 1)\sqrt{D^2 + \rho^2}} \tag{13}$$

for the surface potential distribution as a function of radius $\rho = \sqrt{x^2 + y^2}$ in cylinder coordinates. Figure 9 shows the local surface potential distribution generated by a single elementary charge trapped in silicon ($\varepsilon_m \approx 12.1$). A single elementary charge located 1 nm below the surface will increase the local surface potential by more than 400 mV.

Generation and imaging of trapped surface charges

The generation and imaging of localized charges on an insulating surface was first performed by Stern *et al.*[13] and Terris *et al.*[14] They applied a short voltage pulse between a conducting AFM tip and the sample surface to generate trapped surface charges while scanning the tip in non-contact mode over an insulating surface. In a second scan they could detect these surface charges due to the Coulomb attraction of the 'written' charge to its image charge in the tip. Since those initial experiments, considerable work on suitable substrates and fast readout techniques for high-density data storage has been done.[15,16] Recently, it was also suggested that trapped charges might be used to promote and localize self-assembly processes.[12]

To prove the capability of our KFM microscope to detect trapped charges, we generated different charge patterns on an Si–SiO substrate (0.001 Ω · cm boron-doped silicon with 2–4 nm native oxide on top) by applying short voltage pulses of selectable duration (2.5–400 µs) and amplitudes (10–30 V) between the tip and the sample. Figure 10(a) shows that surface potential and size of the written bits depend on the pulse duration. Bit size and bit stability define whether the substrate is suitable for high-density data storage or not. In our case, bits of 320 nm width could be written

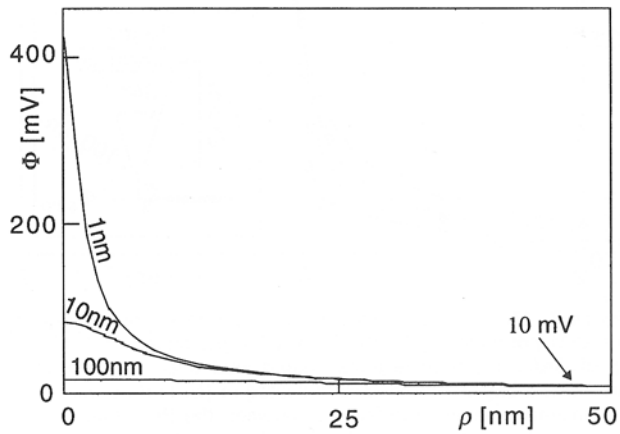

Figure 9. Local surface potential distribution generated by a single elementary charge trapped in silicon ($\varepsilon_m \approx 12.1$) at a distance $D = 1$, 10 and 100 nm below the surface. A single elementary charge located 1 nm below the surface increases the local surface potential by more than 400 mV.

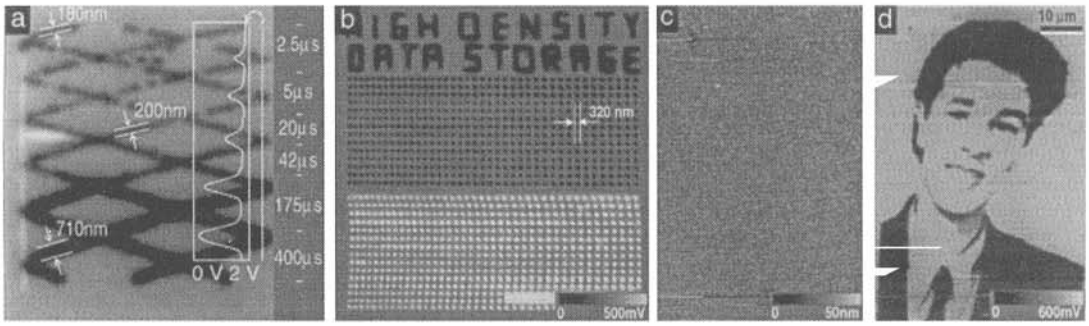

Figure 10. KFM potential images of different generated charge patterns on an Si–SiO substrate. Surface potential and size of the written bits depend on the pulse duration as illustrated in (a). Using 20 µs short pulses, reproducible charge patterns can be generated that remain more than 4 h on the surface without strong degradation (b). A 260 × 360 pixel bit-map image written under computer control on an area of 53 µm × 75 µm is shown in (d). The topography image of the same region (c) illustrates that no cross-talk can be observed between the images.

reproducibly with 20 µs short voltage pulses of 18 V amplitude. The trapped charges could still be imaged 4 h later, although all measurements were taken in air at ambient pressure and humidity [Fig. 10(b)]. However, 24 h later substantial degradation of the charge patterns could be observed. Rinsing the substrate with ultrapure water removed all charges from the surface. This type of voltage pulsing can also be used to generate complex charge patterns, as illustrated in Fig. 10(d) where a 260 × 360 pixel bit-map image was written on an area of 53 µm × 75 µm. The topography image of the same region [Fig. 10(c)] indicates that no cross-talk is present.

Acknowledgements

We thank H. F. Knapp for fruitful discussions, P. Leuchtmann for providing the MMP simulation program and sharing his expertise with its use, O. J. Homan for fabricating the HEMT structures and M. Moser, CSEM Zurich, for donating epitaxially grown heterostructures. Financial support from ETH Zurich and the Swiss National Science Foundation, grant no. 4036-044062, is gratefully acknowledged.

REFERENCES

1. P. Muralt and D. W. Pohl, *Appl. Phys. Lett.* **48**, 514 (1986).
2. P. Muralt, H. Meier, D. W. Pohl and H. W. M. Salemink, *Appl. Phys. Lett.* **50**, 1352 (1987).
3. Y. Martin, D. W. Abraham and H. K. Wickramasinghe, *Appl. Phys. Lett.* **52**, 1103 (1988).
4. J. M. R. Weaver and D. W. Abraham, *J. Vac. Sci. Technol. B* **9**, 1559 (1991).
5. M. Nonnenmacher, M. P. O'Boyl and H. K. Wickramasinghe, *Appl. Phys. Lett.* **58**, 2921 (1991).
6. A. Kikukawa, S. Hosaka and R. Imura, *Appl. Phys. Lett.* **66**, 3510 (1995).
7. M. Yasutake, *Jpn. J. Appl. Phys.* **34**, 3403 (1995).
8. A. Chavez-Pirson, O. Vatel, M. Tanimoto, H. Ando, H. Iwamura and H. Kanbe, *Appl. Phys. Lett.* **67**, 3069 (1995).
9. M. Arakawa, S. Kishimoto and T. Mizutani, *Jpn. J. Appl. Phys.* **36**, 1826 (1997).
10. M. Fujihira and H. Kawate, *J. Vac. Sci. Technol. B* **12**, 1604 (1994).
11. S. Yamashina and M. Shigeno, *J. Electron Microsc.* **44**, 462 (1995).
12. W. M. D. Wright and D. G. Chetwynd, *Nanotechnology* **9**, 133 (1998).
13. J. E. Stern, B. D. Terris, H. J. Mamin and D. Rugar, *Appl. Phys. Lett.* **53**, 2717 (1988).
14. B. D. Terris, J. E. Stern, D. Rugar and H. J. Mamin, *Phys. Rev. Lett.* **63**, 2669 (1989).
15. R. C. Barrett and C. F. Quate, *Ultramicroscopy* **42–44**, 262 (1992).
16. B. D. Terris, R. C. Barrett and H. J. Mamin, *SPIE* **1855**, 194 (1993).
17. H. O. Jacobs, H. F. Knapp, S. Müller and A. Stemmer, *Ultramicroscopy* **69**, 39 (1997).
18. H. O. Jacobs, H. F. Knapp and A. Stemmer, *Rev. Sci. Instrum.*, in press.
19. H. O. Jacobs, P. Leuchtmann, O. J. Homan and A. Stemmer, *J. Appl. Phys.* **84**, 1168 (1998).
20. Ch. Hafner, *The Generalized Multipole Technique for Computational Electromagnetics*. Artech House Books, Boston (1990). The MMP source code is available upon request from P. Leuchtmann (E-mail: leuchtmann@ifh.ee.ethz.ch).
21. M. Gnos, *PhD Thesis*, No. 12158. ETH, Zurich (1997).
22. P. Leuchtmann, in *Proc. URSI Int. Symp. on Electromagnetic Theory*, Thessaloniki, Greece, p. 262 (1998).
23. J. D. Jackson, *Classical Electrodynamics*. Wiley, New York (1975).